Constructing tri-functional modification for spinel $LiNi_{0.5}Mn_{1.5}O_4$ *via* fast ion conductor

Li Li,[a,1] Rui Zhao,[a,1] Du Pan,[a] Shuhong Yi,[a] Liufei Gao,[a] Guanjie He,[c] Huiling Zhao,[a] Caiyan Yu*[a,b] and Ying Bai*[a]

[a] *School of Physics & Electronics, Henan University, Kaifeng 475004, P.R. China.*

[b] *National Demonstration Center for Experimental Physics and Electronics Education, School of Physics and Electronics, Henan University, Kaifeng 475004, PR China.*

[c] *Materials Research Centre, UCL Department of Chemistry, Christopher Ingold Building, 20 Gordon Street, London, WC1H 0AJ, UK.*

*Corresponding author. Tel.: +86-0371-23881602; 13781181979

E-mail: cyyu@henu.edu.cn (Caiyan Yu); ybai@henu.edu.cn (Ying Bai)

Supplementary material: Figure S1-S5, Table S1.

Abstract: Instable surface structure and low capacity retention hinder the further application of high voltage $LiNi_{0.5}Mn_{1.5}O_4$ (LNMO) cathode in lithium-ion battery. In order to promote its electrochemical performances, $Li_{6.4}La_3Al_{0.2}Zr_2O_{12}$ (LLAZO) with the intrinsic property of fast ion conductivity has been employed as a protective layer to modify surface of LNMO. By regulating the LLAZO contents, 1 wt. % LLAZO coated LNMO (LLAZO-1) cathode shows a high capacity of 92.1 mAh g^{-1} over 600 cycles with a capacity retention of 72.6 % at 1 C and a reversible capacity of 57.9 mAh g^{-1} at 20 C, much higher than those of pristine LNMO. Further investigation indicates that the greatly improved electrochemical performances of LLAZO-1 can be attributed to the LLAZO modification, which including the LLAZO surface coating

and La^{3+} and Zr^{4+} gradient co-doping. In addition, the LLAZO precursor significantly restricts the growth of LNMO precursor particles during calcination process, shorting Li^{+} migration pathway. Thus, modification strategy effectively improves the structure stability of LNMO, accompanied with the enhancement in lithium-ion diffusion kinetics performances and confinement in particle growth. This optimization approach with tri-functions sheds light on novel electrode design and construction in rechargeable batteries.

Keywords: *Lithium-ion batteries;* $LiNi_{0.5}Mn_{1.5}O_4$*;* $Li_{6.4}La_3Al_{0.2}Zr_2O_{12}$*; Tri-functional modification.*

1. Introduction

Design of advanced lithium-ion batteries (LIBs) with high specific energy, long cycling life, and low cost is urgently needed for the past few years due to the ever-growing of markets in large-scale electric vehicles and portable electronics and effects of warming.[1-4] However, traditional LIBs are confined to its relatively low operating voltage and poor rate capacities, which are crucial factors to restrict to the further progress of next-generation electric vehicles (EVs) and hybrid electric vehicles (HEVs).[5-6] Thus, LIBs with high energy density are expected to apply in EVs and electronics in the next few years.[7-8] It is generally agreed that working voltage and specific capacity of cathode material are main factors for designing high energy density lithium batteries.[9] Therefore, many efforts have been devoted to explore appropriate cathode materials with the large specific capacity, high voltage and long

cycling.[10-13]

$LiNi_{0.5}Mn_{1.5}O_4$ (LNMO) as the most promising cathode material for the next generation LIBs has high energy and power density, larger theoretical capacity of 147 mAh g^{-1} and fast three-dimensional Li^+ diffusion channel.[14] Therefore, it could offer higher energy density than that of commercially available of $LiCoO_2$ and $LiFePO_4$, 20% and 30% respectively.[15-17] The spinel LNMO has two different crystallographic structures : one is the ordered space group of $P4_332$, in which the Mn^{4+} and Ni^{2+} occupy the 12*d* and 4*a* sites, respectively. Another one is the disordered space group of *Fd3m* with a random distribution of Mn^{4+} and Ni^{2+} in the 16*d* sites and a little amount of Mn^{3+}.[3, 18] It has been reported that the existence of Mn^{3+} could enhance the electrical conductivity and electrochemical performances of LNMO.[19] However, low ionic conductivities of LNMO will lead to its poor rate capability.[20-21] To satisfy the requirements for high power systems, it is of vital importance to realize fast Li^+ insertion-extraction kinetics and structure stability during cycling to improve the rate property of LNMO cathode.[22-23] According to previous reports, reducing the particle size of electrode materials might be an effective way to facilitate the electrode knietics performances owing to the drastically shortened diffusion paths for ion and electron.[24-27] Nevertheless, nano-metric LNMO may exhibit accelerated electrolyte decomposition and Mn dissolution under high potential, which leads to low coulombic effciency and poor cyclic performance.[23, 28-29] Besides, at elevated temperatures, the high-voltage LNMO material suffers from a limited cycle life, basically owing to surface structure distortion and side reactions happened at interface

between cathode material and electrolyte.[30-33] Many studies reported the degradation mechanism of high-voltage LNMO during charge-discharge process.[32] Previous studies showed that the direct contact between electrode materials and organic electrolyte would cause transition metal (TM) dissolution and electrolyte decomposition, which could increase the thickness of solid-electrolyte interface (SEI) film, and thus hinder the electrochemical performance.[34-37] In addition, the dissolution of TM is always from surface into interior of LNMO, and thus robust surface structure is critical in protecting the LNMO material from structure degradation as well as promoting its electrochemical performances and thermal stability at elevated temperatures.[38]

To suppress the above-mentioned disadvantages on surface of cathode materials and obtain excellent electrochemical performances for applications, surface modification is currently one of the most widely used strategies.[39-41] In recent years, Li^+ conductive materials, including $LiAlSiO_4$[42], Li_3PO_4[43], Li_2SiO_3[44], $LiNbO_3$[45] *etc.*, have been widely utilized as coating layer to modify high-voltage cathode material and proved to be a feasible way to improve the rate capability of LNMO and inhibit side reaction. However, these Li^+ conductive materials are not advantageous in future all-solid-state batteries, because of its narrowed voltage windows and low Li^+ conductivity. Furthermore, the garnet structure fast ion conductor $Li_7La_3Zr_2O_{12}$ has a wide voltage window and high ionic conductivity is the most promising candidate material for solid electrolytes, and was applied to coat $LiMn_2O_4$ and $Li_3V_2(PO_4)_3$, proving that coating layer of Li^+ conductor contribute to enhance stability of material

and accelerate the diffusion of Li^+.[46-47] Therefore, we have chosen the $Li_{6.4}La_3Al_{0.2}Zr_2O_{12}$ (LLAZO) with cubic phase, Al^{3+} doping stablized the cubic phase and improved the ionic conductivity, to coat the surface of LNMO precursor and hoped it can not only provide the protective layer, but also provide an optimization method for the interface problem of all solid-state batteries.[48-50] As an alternative strategy for modifying LNMO cathode material, elemental doping such as Cr^{3+}, Al^{3+}, Ti^{4+}, Si^{4+}, Nb^{5+} and P^{5+}, could effectively improve the spinel LNMO electrochemical properties including rate performance and cyclic stability by minimizing polarization, suppressing TM ions dissolution and improving ionic/electronic conductivities.[10, 51-56]

In this work, we concentrated on designing a tri-functioal modification strategy, by employing $Li_{6.4}La_3Al_{0.2}Zr_2O_{12}$ (LLAZO) precursor (Li, Al, La, Zr based salts) to coat LNMO precursor powders followed by calcination at 820 ^oC to form the coating layer and LNMO material simultaneously.[57-58] In this case, LLAZO coating layer restricts the growth of LNMO precursor particles during crystalization process.[59] Moreover, it is expected that alien ions will diffuse into the lattice of LNMO. In previous reports, the doping of atoms has been frequently found for surface coating method, and La and Zr ions penetrate into the LNMO lattice are prove to improve the structural stability of LNMO.[56, 60-65] The LLAZO coating layer on the surface of LNMO precursor in this work was supposed to lead to a gradient diffusion of La and Zr ions into the LNMO lattice during calcination process at 820 ^oC. As a result, a modified LNMO cathode with superior cycling stability and rate performance was obtained.

2. Experimental section

2.1. Synthesis of LNMO

Spinel LNMO was prepared via a sol-gel method. In a typical synthesize process, $LiCH_3COO$ (99 %), $Ni(CH_3COO)_2{\cdot}4H_2O$ (99 %) and $Mn(CH_3COO)_2{\cdot}4H_2O$ (99 %), and citric acid (99.5 %) were dissolved sperately into distilled water. Next, these solutions were homogeneously mixed with stirred vigorously to form a transparent sol and following evaporated at 80 ^oC. During the evaporation process, the ammonium hydroxide solution was dropwise added to adjust the pH value of mixed solution to around 6.5. Afterwards, the sol was dried at 120 ^oC for 24 h in a drying oven to form the corrresponding dried gel. Subsequently, the dried gel was complete ground and pre-heated at 500 ^oC for 6 h to form LNMO precusor. Finally, the prepared precurosr was further calcined at 820 ^oC for 14 h to obtain pristine LNMO material.

2.2 Synthesis of LLAZO-modified LNMO

To synthesize the LLAZO-modified LNMO samples, first, stoichiometric amounts of LNMO precursor powders were dispersed into ethyl alcohol solution. After that, stoichiometric amount of $LiNO_3$ (99 %), $Al(NO_3)_3{\cdot}9H_2O$ (99 %), $La(NO_3)_4{\cdot}4H_2O$ (99 %) and $Zr(NO_3)_3{\cdot}5H_2O$ (99 %) solutions were dropwise added to alcohol solution. Then, the mixed solution was evaporated at 65 ^oC to form a sol and following dried at 90 ^oC for overnight to obtain the dried gel. Finally, dried gel was ground and calcined at 820 ^oC for 14 h in the air to obtain the LLAZO-modified LNMO materials. The amount of coated LLAZO corresponded to 0, 1, 2, and 3 wt. % of the LNMO samples, and the obtained a serious of samples are denoted as pristine, LLAZO-1, LLAZO-2,

LLAZO-3, respectively.

2.3 Materials characterization

The crystal structures of all prepared materials were characterized by X-ray diffraction (XRD, Bruker D8 Advance) with a Cu Kα radiation source under the range of 10° and 120° (2θ). The Rietveld refinement data of the powder diffraction was obtained by using Fullprof suite software. The Raman spectra were carried out by a laser Raman spectrometer (RM-1000, Renishaw) with a 633 nm He-Ne laser. The contents of elements analysis were detected by an inductively coupled plasma spectrometer (ICP, Thermo Fisher ICAP 6300). The surface morphologies and particle sizes were collected with scanning electron microscope (SEM, JSM-7001F). Transmission electron microscopy (TEM) and high-resolution TEM (HRTEM) images were obtained on a FEI G2 F20 instrument. The electron energy loss spectroscopy (EELS) analysis and scanning transmission electron microscopy (STEM) were performed using a JEM-ARM200F microscope, which was equipped with a spherical-aberration corrector and Gatan image filter. Energy-dispersive X-ray spectroscopy (EDS) elemental mapping images were collected on a Talos F200 X (FEI) instrument. The surface element chemical environment were acquired by used a X-ray photoelectronioc spectrometer (XPS, ESCALAB 250, Thermo Fisher Scientific). The XPS data were analysized by using CasaXPS software.

2.4 Electeochemical characterizations

Electrochemical performance was tested using CR2032-type coin cells with the metal Li as the counter electrode and Calgary 2500 porous polypropylene film served as the

separator. The active materials, acetylene black, and polyvinylidene fluoride (PVDF) were mixed with a mass ratio of 8:1:1 in N-methyl-2-pyrrolidone (NMP) solvent to form a slurry. After then, the mixed slurry was uniformly spread on an Al foil and dried at 110 °C for 12 h. Coin cells were assembled in an glovebox (argon-filled) and tested on a LAND-CT2001A test system at different current densities in voltage range of 3.5-4.9 V at temperatures (25 ^{o}C and 55 ^{o}C). Electrochemical impedance spectroscopy (EIS) and cyclic voltammetry (CV) were perform on a CHI660E (Shanghai, Chenhua) electrochemical workstation.

3. Results and discussion

The synthesis process of LLAZO-modified LNMO cathode material is schematically illustrated in Figure 1. Firstly, the LNMO precursor was obtained via sol-gel method and pre-treatment at 500 ^{o}C. After that, the contain Li, Al, La, Zr-based salts and citric acid were mixed with the LNMO precursor in ethyl alcohol solution, followed by evaporating at 65 ^{o}C to obtain the precursors of LLAZO-modified LNMO cathode sample. Finally, the obtained precursor powders were calcined at 820 ^{o}C for 14 h to complete the crystallization process, and various amounts of LLAZO layers were successfully formed on the LNMO surface.

3.1 Sample characterization

The XRD patterns of LNMO and LLAZO-modified LNMO samples are shown in Figure 2a, in which diffraction peaks of all materials are in consistent with disordered space group of *Fd3m*.[66] Along with the increased LLAZO contents on LNMO surface,

the position of diffraction peaks shifted to the lower 2-theta values (in the right enlarged pattern). The fact indicates that the lattice parameters of all samples are linear increased. To further investigate the variation of LNMO phase structure after LLAZO modifying, the lattice parameters of all samples were calculated through the Rietveld refinement method (Figure S1), and the data are listed in Table S1. It could testified that cell volume and lattice parameter of all samples are increased along with the amount of LLAZO on LNMO surface. It has been reported that the radius of Mn^{3+} (0.645 Å) is larger than that of Mn^{4+} (0.530 Å), so the lattice parameter increase of LNMO after LLAZO modifying is mainly caused by foreign ions migrating into the lattice of LNMO from coating layer, which could lead the transform of Mn^{4+} to Mn^{3+}.[67]

In Figure S2, the Raman spectra of all materials were compared to investigate the local structure change of LNMO. According to previous studies, the peak located at 630 cm^{-1} could be attributed to the symmetric Mn-O stretching mode (A_{1g}) in the MnO_6 octahedron of LNMO.[68] Both peaks at 396 and 493 cm^{-1} were originated from the Ni^{2+}-O stretching.[14, 68] The peak T_{2g} without splitting located at around 587 cm^{-1} was deemed to be the characteristic of Fd3m space group. For LLAZO modified LNMO materials, the band positions of Mn–O and Ni–O bonding shifted to lower wavenumbers indicating the decreasing of Mn oxidation states.

Surface morphologies of pristine, LLAZO-1, LLAZO-2, and LLAZO-3 were displayed in Figure 2b_1-b_4. All materials exhibit a uniform distribution of truncated octahedron particles and their particle sizes decreasing with increasing of LLAZO

modifying content. As the amount of LLAZO increases, the average particle sizes of pristine, LLAZO-1, LLAZO-2, and LLAZO-3 are 321, 204, 147 and 139 nm, respectively (Figure 2b_1-b_4, inset), indicating that the LLAZO precursor can restrict the particle growth of LNMO during the calcination process. This phenomenon may be caused by the LLAZO precursor on the surface of the LMNO precursor particles, which acts as a separation network during calcination, limiting the particles of LNMO precursors from contacting each other and forming larger particles. After LLAZO modification, the smaller particle of LNMO has a shorter Li^+ diffusion path, which helps to improve the kinetic behavior.

To analyze the surface chemical environment of the as-prepared materials, XPS measurement were performed and the results are shown in Figure S3. For LLAZO-modified LNMO samples, XPS spectra of La *3d*, Zr *3d* and Al *2p* were observed on surface of material. If foreign ions diffuse into the LNMO crystal lattice during calcination process, foreign ions break the surrounding chemical environment and the oxidation state of Mn ions is reduced from +4 to +3 to satisfy the principle of charge neutrality, because the Ni^{2+} ions in the LNMO lattice are virtually impossible to further reduce. Therefore, to more accurately determine the oxidation state of Mn ions, the binding energy of Mn 2p in all samples was analyzed in Figure S4. The Mn *2p* spectrum including two peaks located at ~ 643 and 654 eV, which are usually identified to Mn $2p_{3/2}$ and Mn $2p_{1/2}$, and each peak could be further fitted into two separate peaks based on the MnO_2 and Mn_2O_3 lines, indicating the coexistence of Mn^{3+} and Mn^{4+}. The Mn^{3+} percentage content calculated by the peak areas of all

samples is 50.5 %, 57.8 %, 62.5 % and 71.2 %, respectively. The Mn^{3+} percentages of LNMO-LLAZO samples are obviously increased than pristine, indicating the transformation from Mn^{4+} to Mn^{3+} after LLAZO modification. A detailed study of the relationship between electrochemical performance and content of Mn^{3+} indicating an appropriate amount of Mn^{3+} is considered crucial for Li^{+} transport inside the crystalline lattice and rate capacity of LNMO.[69] As shown in Figure 2c1-c4, in order to conclusively prove that the foreign ions diffused into the spinel LNMO lattice, the XPS sputtered depth analysis was performed for LLAZO-1. With surface layer removed by Ar beam sputtering, the XPS signals of interior particle can be collected with an etching time of 30 s everytime and corresponding the probe depth about ~ 7nm. Figure 2c_1 and c_2 exhibit that the signal intensities of the Mn *2p* and Ni *2p* elements increase with increasing of etching time, while that of La *3d* and Zr *3d* monotonically decrease (Figures 2c_3 and c_4). The gradual decay of La *3d* and Zr *3d* signals in XPS implies the gradient doping of La^{3+} and Zr^{4+} in LLAZO-1 cathode material. The results indicate that the of La^{3+} and Zr^{4+} from coating layer diffuse and substitute into the spinel LNMO crystal lattice during the calcination process. According to previous reports and our obtained data, it is suggested that the amorphous LLAZO coating layer successfully exists on the surface of LNMO and the La and Zr ions gradient dope into the LNMO.

TEM and HRTEM images were used to describe the detailed structure information of pristine and LLAZO-1 samples. Figure 3a, b and c shows details for the pristine LNMO and Figure 3e, f and j for the LLAZO-1 sample. Both samples

show the lattice fringes with the interplanar spacing of ~ 0.47 nm, which corresponds to {111} plane of LNMO. The sharp edge with the clear lattice fringe reaching to the grain boundary could be observed in Figure 3c, implying perfect crystallization of the pristine sample. As shown in Figure 3j, the LLAZO-1 sample exhibits an amorphous LLAZO coating layer (about 4 nm), which could be deem to well adhered to the surface of LNMO material during the synthetic process. Their corresponding FFT patterns (Figure 3h) of marked regions 2 and 3 in Figure 3j can further confirm the different crystallization degree between LNMO and coating layer. The amorphous coating layer is believed to be advantageous in alleviating the lattice mismatch in terms of both ion transport and lattice strain around the grain boundary. Therefore, the amorphous ultrathin coating layer that contained Li allowed lithium ions to diffuse freely, which lead to an enhanced rate capability. To provide more information of the coating layer, the EELS signals were collected for the selected rectangular in the thin coating layer, which clearly proves the existence of La and Zr elements (Figure S5). This result from one viewpoint confirms the deposition of LLAZO on the surface of LNMO particle. Besides, the EDS mapping images (Figure 3i) reveal that the elements of La, Zr and Al are uniformly existed in the LNMO. All results further indicating that an amorphous LLAZO layer was formed on surface of LNMO particles. The contents of LLAZO in 1, 2 and 3 wt.% LLAZO modified LNMO materials were respectively determined to be 0.94, 1.82 and 2.72 wt.% by utilizing ICP analysis.

3.2. Electrochemical measurements

The galvanostatic charge-discharge test curves for the first cycle were conducted at the current density of 14.7 mA g^{-1} (0.1 C) in the range from 3.5 V to 4.9 V at 25 ºC. As could be observed in Figure 4a, all assembled cathode electrodes displayed two characteristic voltage plateaus: one long and obvious voltage plateau ~ 4.7 V arising from the $Ni^{2+/4+}$ redox process, and another short voltage plateau ~ 4.0 V attributed to the $Mn^{3+/4+}$ redox reaction, which is originated from the disordered Fd3m phase. The length of charge-discharge plateaus (~ 4.0 V) increases along with increasing of LLAZO coating content, which indicating the increasing of Mn^{3+} content in LNMO materials. The reversible specific discharge capacities of pristine, LLAZO-1, LLAZO-2 and LLAZO-3 are 122.8, 127.3, 120.0, and 118.7 mAh g^{-1}, respectively. Besides, the first-cycle coulombic efficiency of the pristine, LLAZO-1, LLAZO-2 and LLAZO-3 electrodes are calculated to be 82.7 %, 80.9 %, 79.7 % and 79.4 %. The decreasing of coulombic efficiency could be mainly ascribed to the decrease of particle size after LLAZO modification, which will inevitably induce more side reactions in the first cycle with higher specific surface areas. Figure 4b compares the rate capabilities of all materials at different current densities from 0.1 to 20 C, and the improved rate capability proves the advantage of LLAZO modifying layer. At the low and moderate discharge rates (0.1 to 2 C), all electrode material exhibit similar discharge capacities. Through comparison, at 5 to 20 C, the bare LNMO material shows inferior discharge capacity, while LLAZO-modified LNMO materials keep higher discharge capacity. For example, at current density of 20 C, LLAZO-1, LLAZO-2 and LLAZO-3 electrodes exhibit discharge capacities of 57.9, 23.6, and

17.7 mAh g^{-1}, while bare LNMO electrode shows an extremely low discharge capacity (~ 0 mAh g^{-1}). Noteworthily, the LLAZO-1 delivers the best capacity retention at each current density among all samples. Figure 4c compares the cycling performances and coulombic efficiency of all electrodes at rate of 1 C over 600 cycles at 25 ºC. Clearly, the pristine LNMO cathode material remains only 45.8 % of its first discharge capacity, fading from 122.8 to 56.2 mAh g^{-1} after 600 cycles. Although, the LLAZO-1, LLAZO-2, and LLAZO-3 electrodes show improved capacity retentions of 72.6, 69.8, and 54.1 % after 600 cycles and with more stable coulombic efficiency. Particularly, the LLAZO-1 delivers the highest capacity retention and largest discharge capacity after 600 cycles among all samples. Even at 55 ºC (0.1 C, 14.7 mA g^{-1}), the LLAZO modified LNMO sample could still remain a better initial discharge capacity and a higher retention than pristine LNMO sample (Figure 4d). Although all samples show a rapid decrease in capacity due to dissolution of TM in the electrolyte and formation of a relatively thick SEI layer at high temperatures, the LLAZO modified LNMO samples exhibit higher capacities and longer life spans than pristine material. By comparison, over 100 cycles, the LLAZO-1, LLAZO-2, and LLAZO-3 electrode materials exhibit enhanced capacity retentions of 74.4 %, 72.3 %, and 72.5 % after 100 cycles than that of pristine LNMO (24.5 %). At the same time, the LLAZO-modified LNMO materials have higher coulombic efficiencies compared with the bare electrode, which could be traced to LLAZO coating layer and gradient doping of La^{3+} and Zr^{4+} ions improving the structure stability of LNMO.

A series of (CV) measurements were carried out to investigate Li^{+} kinetics

behavior in pristine LNMO and LLAZO-1 materials. Figure 5a-b show that their CV curves at a different scan rates. During charge-discharge process, the insertion/extraction reaction is controlled by the solid-state diffusion of Li^+, as increasing of scan rate (v), the peak current (i_p) is enhanced and voltage separation is broadened. The diffusion coefficient of Li^+ ions can be calculated according to the Randles−Sevcik equation as following:[70]

$$i_p = \left(2.69\times10^5\right)n^{3/2}AD_{Li}^{1/2}v^{1/2}\Delta C_{Li}$$

Compared to the pristine LNMO, the LLAZO-1 material reduces the polarization between the oxidation and reduction peaks of Ni^{2+} and Ni^{3+}. According to the slope of linear fit, the values of Li^+ diffusion coefficients were calculated. The LLAZO-1 sample presents a higher diffusion coefficient of D_{Li} (3.35×10^{-11} cm^2 s^{-1}) compared with that of pristine material (2.73×10^{-12} cm^2 s^{-1}). The results undoubtedly testify the Li^+ diffusion at interface was notably enhanced by LLAZO modification layer.

Figure 5c and d show the Nyquist plots of the pristine and LLAZO-1 composites after different cycles. To further illustrate the different ohmic polarization, the EIS measurement was carried out at fully charged state (4.9 V), and the equivalent circuit was shown in the inset in Figure 5c. The intercept of Z'-axis at the high frequency region represents ohmic resistance (R_s) of the cell, and it is relatively small compared to other resistances come from cathode material. The first semicircle at high frequency region is correlated to the Li^+ diffusion across the surface layer (R_{sf}). The second semicircle, at medium-to-low frequency, which is ascribed to the charge transfer resistance (R_{ct}) at the electrode-electrolyte interface. A slopping line at low

frequency region is attributed to the Warburg impedance of Li^+ diffusion in the bulk material. The fitting EIS parameters of both samples were provided in Table 1, in which the pristine and LLAZO-1 cathode electrodes have the similar R_s values. While after same cycle times, the LLAZO-1 has the lower resistances of Li^+ diffusion than pristine. Apparently, the result indicated that the fast ion conductor LLAZO coating somehow suppress the fast increase of R_{sf}, which will facilitate the diffusion of Li^+ and electron at interface and explains the improved electrochemical performances to some extent.

4. Conclusion

In this paper, we successfully obtained a LNMO material with a trifunctional effect of LLAZO modification by coating a precursor of LNMO and then performing a single calcination at 820 ºC. The tri-functional effects were presented in Figure 6 and summarized as follows: (i) LLAZO coating layer on surface of LNMO particles act as protective layer, (ii) gradient doping of La^{3+} and Zr^{4+} ions into the LNMO lattice to generate Li-La-Al-Zr-O solid solution transition layer could facilitate Li^+ transportation at the interface, (iii) the LLAZO precursor restricts the growth of LNMO precursor particles, leading a shorted Li^+ migration pathway. In comparison, the LLAZO-1 shows improved capacity retention of 72.6% after 600 cycles with an excellent capacity and prominent rate capacity at 20 C (57.9 mAh g^{-1}). In addition, even at 55 °C, the LLAZO-1 exhibits improved cycling stability compared to that of pristine sample. Therefore, coating solid electrolyte $Li_{6.4}La_3Al_{0.2}Zr_2O_{12}$ is a feasible strategy to enhance the electrochemical properties of LNMO cathode materials by

tri-functional modification effects. In this paper, we also design a novel method to prepared a compatible interface between LLAZO solid electrolyte and LNMO active electrode, which provides a new idea for solving the bottleneck of solid-state interface compatibility.

Conflicts of interest

There are no conflicts to declare.

Author Contributions

[1] Li Li and Rui Zhao contributed equally.

Acknowledgements

This work is supported by the National Natural Science Foundation of China (NSFC) (50902044, 51672069), the Program for Innovative Research Team in Science and Technology in University of Henan Province (IRTSTHN) (20IRTSTHN012), the Foundation of Henan Educational Committee (18A140001) and Science and Technology Development Project of Henan Province (192102210235).

References

(1) J.Y. Piao, Y.G. Sun, S.Y. Duan, A.M. Cao, X.L. Wang, R.J. Xiao, X.Q. Yu, Y. Gong, L. Gu, Y. Li, Z.J. Liu, Z.Q. Peng, R.M. Qiao, W.L. Yang, X.Q. Yang, J.B. Goodenough, L.J. Wan, Stabilizing cathode materials of lithium-ion batteries by controlling interstitial sites on the surface, Chem 4 (2018) 1685-1695.

(2) L. Xing, X. Zheng, M. Schroeder, J. Alvarado, W.C.A. Von, K. Xu, Q. Li, W. Li,

Deciphering the ethylene carbonate-propylene carbonate mystery in Li-ion batteries, Acc. Chem. Res. 51 (2018) 282-289.

(3) A. Manthiram, K. Chemelewski, E.S. Lee, A perspective on the high-voltage $LiMn_{1.5}Ni_{0.5}O_4$ spinel cathode for lithium-ion batteries, Energy Environ. Sci. 7 (2014) 1339-1350.

(4) J.Y. Xia, S.Q. Wan, Independent effects of warming and nitrogen addition on plant phenology in the Inner Mongolian steppe, Annals of Botany 111 (2013) 1207-1217.

(5) X.B. Cheng, R. Zhang, C.Z. Zhao, F. Wei, J.G. Zhang, Q. Zhang, A review of solid electrolyte interphases on lithium metal anode, Adv. Sci. 3 (2016) 1500213-1500233.

(6) J. Qian, L. Liu, J. Yang, S. Li, X. Wang, H.L. Zhuang, Y. Lu, Electrochemical surface passivation of $LiCoO_2$ particles at ultrahigh voltage and its applications in lithium-based batteries, Nat. Commun. 9 (2018) 4918-4929.

(7) F. Wang, L. Suo, Y. Liang, C. Yang, F. Han, T. Gao, W. Sun, C. Wang, Spinel $LiNi_{0.5}Mn_{1.5}O_4$ cathode for high-energy aqueous lithium-ion batteries, Adv. Energy Mater. 7 (2017) 1600922-160928.

(8) W. Li, X. Liu, H. Celio, P. Smith, A. Dolocan, M. Chi, A. Manthiram, Mn versus al in layered oxide cathodes in lithium-ion batteries: a comprehensive evaluation on long-term cyclability, Adv. Energy Mater. 8 (2018) 1703154-1703165.

(9) T. Dong, J. Zhang, G. Xu, J. Chai, H. Du, L. Wang, H. Wen, X. Zang, A. Du, Q. Jia, X. Zhou, G. Cui, A multifunctional polymer electrolyte enables ultra-long

cycle-life in a high-voltage lithium metal battery, Energy Environ. Sci. 11 (2018) 1197-1203.

(10) J. Wang, P. Nie, G.Y. Xu, J.M. Jiang, Y.T. Wu, R.R. Fu, H. Dou, X.G. Zhang, High-voltage $LiNi_{0.45}Cr_{0.1}Mn_{1.45}O_4$ cathode with superlong cycle performance for wide temperature lithium-ion batteries, Adv. Funct. Mater. 28 (2018) 1704808-1704817.

(11) L. Zhou, D. Zhao, X. Lou, $LiNi_{0.5}Mn_{1.5}O_4$ hollow structures as high-performance cathodes for lithium-ion batteries, Angew. Chem. In.t Ed. 51 (2012) 239-241.

(12) P. Yan, J. Zheng, J. Liu, B. Wang, X. Cheng, Y. Zhang, X. Sun, C. Wang, J.G. Zhang, Tailoring grain boundary structures and chemistry of Ni-rich layered cathodes for enhanced cycle stability of lithium-ion batteries, Nature Energy 3 (2018) 600-605.

(13) W. Yan, Y. Liu, S. Guo, T. Jiang, Effect of defects on decay of voltage and capacity for $Li[Li_{0.15}Ni_{0.2}Mn_{0.6}]O_2$ cathode material, ACS Appl. Mater. Interfaces 8 (2018) 12118-12126.

(14) M. Börner, P. Niehoff, B. Vortmann, S. Nowak, M. Winter, F.M. Schappacher, Comparison of different synthesis methods for $LiNi_{0.5}Mn_{1.5}O_4$ influence on battery cycling performance, degradation, and aging. Energy Technol. 4 (2016) 1631-1640.

(15) J. Xiao, X. Chen, P.V. Sushko, M.L. Sushko, L. Kovarik, J. Feng, Z. Deng, J. Zheng, G.L. Graff, Z. Nie, D. Choi, J. Liu, J.G. Zhang, M.S. Whittingham, High-performance $LiNi_{0.5}Mn_{1.5}O_4$ spinel controlled by Mn^{3+} concentration and site disorder, Adv. Mater. 24 (2012) 2109-2116.

(16) J.B. Goodenough, K.S. Park, The Li-ion rechargeable battery: a perspective, J.

Am. Chem. Soc. 135 (2013) 1167-1176.

(17) C.X. Zu, H. Li, Thermodynamic analysis on energy densities of batteries, Energy Environ. Sci. 4 (2011) 2614.

(18) Y. Chen, Y. Sun, X. Huang, Origin of the Ni/Mn ordering in high-voltage spinel $LiNi_{0.5}Mn_{1.5}O_4$: the role of oxygen vacancies and cation doping, Computational Materials Science 115 (2016) 109-116.

(19) L. Wang, H. Li, X. Huang, E. Baudrin, A comparative study of Fd-3m and $P4_332$ "$LiNi_{0.5}Mn_{1.5}O_4$", Solid State Ionics 193 (2011) 32-38.

(20) J. Chong, S. Xun, X. Song, G. Liu, V.S. Battaglia, Surface stabilized $LiNi_{0.5}Mn_{1.5}O_4$ cathode materials with high-rate capability and long cycle life for lithium ion batteries, Nano Energy 2 (2013) 283-293.

(21) T. Yang, N. Zhang, Y. Lang, K. Sun, Enhanced rate performance of carbon-coated $LiNi_{0.5}Mn_{1.5}O_4$ cathode material for lithium ion batteries, Electrochimica Acta 56 (2011) 4058-4064.

(22) S. Yang, J. Chen, Y. Liu, B. Yi, Preparing $LiNi_{0.5}Mn_{1.5}O_4$ nanoplates with superior properties in lithium-ion batteries using bimetal–organic coordination-polymers as precursors, J. Mater. Chem. A 2 (2014) 9322-9330.

(23) A. Ignatiev, X. Chen, N. Wu, Z. Lu, L. Smith, Nanostructured thin solid oxide fuel cells with high power density, Dalton Trans. (2011) 5501-5506.

(24) H. Xu, J. Shu, X. Hu, Y. Sun, W. Luo, Y. Huang, Electrospun porous $LiNb_3O_8$ nanofibers with enhanced lithium-storage properties, J. Mater. Chem. A 1 (2013) 15053-15059.

(25) C. Lv, J. Sun, G. Chen, C. Yan, D. Chen, Achieving $Ni_3V_2O_8$ amorphous wire encapsulated in crystalline tube nanostructure as anode materials for lithium ion batteries, Nano Energy 33 (2017) 138-145.

(26) L. Zhou, K. Zhang, J. Sheng, Q. An, Z. Tao, Y.M. Kang, J. Chen, L. Mai, Structural and chemical synergistic effect of CoS nanoparticles and porous carbon nanorods for high-performance sodium storage, Nano Energy 35 (2017) 281-289.

(27) H. Liu, J. Wang, X. Zhang, D. Zhou, X. Qi, B. Qiu, J. Fang, R. Kloepsch, G. Liu, Z. Schumacher, J. Li, Morphological evolution of high-voltage spinel $LiNi_{0.5}Mn_{1.5}O_4$ cathode materials for lithium-ion batteries: the critical effects of surface orientations and particle size, ACS Appl. Mater. Interfaces 8 (2016) 4661-4675.

(28) D. Kovacheva, B. Markovsky, G. Salitra, Y. Talyosef, M. Gorova, E. Levi, M. Riboch, H.J. Kim, D. Aurbach, Electrochemical behavior of electrodes comprising micro- and nano-sized particles of $LiNi_{0.5}Mn_{1.5}O_4$: a comparative study, Electrochim. Acta 50 (2005) 5553-5560.

(29) K.R. Chemelewski, E.S. Lee, W. Li, A. Manthiram, Factors influencing the electrochemical properties of high-voltage spinel cathodes: relative impact of morphology and cation ordering, Chem. Mater. 25 (2013) 2890-2897.

(30) H.F. Deng, P. Nie, H.F. Luo, Y. Zhang, J. Wang, X.G. Zhang, Highly enhanced lithium storage capability of $LiNi_{0.5}Mn_{1.5}O_4$ by coating with Li_2TiO_3 for Li-ion batteries, J. Mater. Chem. A 2 (2014) 18256-18262.

(31) H. Wang, L.B. Ben, H.L. Yu, Y.Y. Chen, X.A. Yang, X.J. Huang, Understanding the effects of surface reconstruction on the electrochemical cycling performance of

the spinel $LiNi_{0.5}Mn_{1.5}O_4$ cathode material at elevated temperatures, J. Mater. Chem. A 5 (2016) 822-834.

(32) A. Burak, J.L. Matthew, N. Tim, Y. Reza, T. Carl, Z. Wolfgang, B. Daniel, E. Kristina, Understanding the capacity loss in $LiNi_{0.5}Mn_{1.5}O_4$−$Li_4Ti_5O_{12}$ lithium ion cells at ambient and elevated temperatures, J. Phys. Chem. C 122 (2018) 11234-11248.

(33) T. Yoon, S. Park, J. Mun, J.H. Ryu, W. Choi, Y.S. Kang, J.H. Park, S.M. Oh, failure mechanisms of $LiNi_{0.5}Mn_{1.5}O_4$ electrode at elevated temperature, J. Power Sources 215 (2012) 312-316.

(34) X. Fang, M. Ge, J. Rong, C. Zhou, Graphene-oxide-coated $LiNi_{0.5}Mn_{1.5}O_4$ as high voltage cathode for lithium ion batteries with high energy density and long cycle life, J. Mater. Chem. A 1 (2013) 4083-4088.

(35) S.T. Myung, K. Amine, Y.K. Sun, Surface modification of cathode materials from nano- to microscale for rechargeable lithium-ion batteries, J. Mater. Chem. 20 (2010) 7074-7095.

(36) Y.M. Song, J.G. Han, S. Park, K.T. Lee, N.S. Choi, A multifunctional phosphite-containing electrolyte for 5 v-class $LiNi_{0.5}Mn_{1.5}O_4$ cathodes with superior electrochemical performance, J. Mater. Chem. A 2 (2014) 9506-9513.

(37) L. Johannes, P. Daniel, A.G. Hubert, An analysis protocol for three-electrode Li-ion battery impedance spectra: part i. analysis of a high-voltage positive electrode, J. Electrochem. Soc. 164 (2017) A1773-A1783.

(38) D. Hugues, D. Dominique, A.L. Yaser, J.D. Isobel, Study of the

$LiMn_{1.5}Ni_{0.5}O_4$/electrolyte interface at room temperature and 60 ºC, J. Electrochem. Soc. 158 (2011) A537-A545.

(39) T.H. Xu, Y.P. Li, D.D. Wang, M. Wu, D. Pan, H.L. Zhao, Y. Bai, Enhanced electrochemical performance of $LiNi_{0.5}Mn_{1.5}O_4$ cathode material by YPO_4 surface modification, ACS Sustainable Chem. Eng. 6 (2018) 5818-5825.

(40) J.S. Park, X. Meng, J.W. Elam, S. Hao, C. Wolverton, C. Kim, J. Cabana, Ultrathin lithium-ion conducting coatings for increased interfacial stability in high voltage lithium-ion batteries, Chem. Mater. *26* (2014) 3128-3134.

(41) Y.F. Deng, S.X. Zhao, Y.H. Xu, C.W. Nan, Effect of temperature of Li_2O–Al_2O_3–TiO_2–P_2O_5 solid-state electrolyte coating process on the performance of $LiNi_{0.5}Mn_{1.5}O_4$ cathode materials, J. Power Sources 296 (2015) 261-267.

(42) J.C. Deng, Y.L. Xu, L. Li, T.Y. Feng, L. Li, Microporous $LiAlSiO_4$ with high ionic conductivity working as a coating material and water adsorbent for $LiNi_{0.5}Mn_{1.5}O_4$ cathode, J. Mater. Chem. A 4 (2015) 6561-6568.

(43) G.F. Ortiz, M. Cabello, M.C. López, J.L. Tirado, M.J. McDonald, Y. Yang, Exploring a li-ion battery using surface modified titania nanotubes versus high voltage cathode nanowires, J. Power Sources 303 (2016) 194-202.

(44) J. Mou, Y. Deng, Z. Song, Q. Zheng, K.H. Lam, D. Lin, Excellent rate capability and cycling stability in Li^+-Conductive Li_2SnO_3-coated $LiNi_{0.5}Mn_{1.5}O_4$ cathode materials for lithium-ion batteries, Dalton Trans. 47 (2018) 7020-7028.

(45) K. Hyeongwoo, B. Dongjin, C. Wonyoung, G.J. Hun, C. Wonchang, A nano-$LiNbO_3$ coating layer and diffusion-induced surface control towards

high-performance 5 V spinel cathodes for rechargeable batteries, J. Mater. Chem. A 5 (2017) 25077-25089.

(46) Y.F. Deng, S.X. Zhao, Y.H. Xu, C.W. Nan, Effect of the morphology of Li–La–Zr–O Solid Electrolyte Coating on the electrochemical performance of spinel $LiMn_{1.95}Ni_{0.05}O_{3.98}F_{0.02}$ cathode materials, J. Mater. Chem. A 2 (2014) 18889-18897.

(47) J. Zhou, X. Sun, K. Wang, Preparation of high-voltage $Li_3V_2(PO_4)_3$ co-coated by carbon and $Li_7La_3Zr_2O_{12}$ as a stable cathode for lithium-ion batteries, Ceram. Inter. 42 (2016) 10228-10236.

(48) Y. Matsuda, K. Sakamoto, M. Matsui, O. Yamamoto, Y. Takeda, N. Imanishi, Phase formation of a garnet-type lithium-ion conductor $Li_{7-3x}Al_xLa_3Zr_2O_{12}$, Solid State Ionics 277 (2015) 23-29.

(49) L. Miara, A. Windmuller, C.L. Tsai, W.D. Richards, Q. Ma, S. Uhlenbruck, O. Guillon, G. Ceder, About the compatibility between high voltage spinel cathode materials and solid oxide electrolytes as a function of temperature, ACS Appl. Mater. Interfaces 8 (2016) 26842-26850.

(50) L.N. Wu, J. Peng, Y.K. Sun, F.M. Han, Y.F. Wen, C.G. Shi, J.J. Fan, L. Huang, J.T. Li, S.G. Sun, High-energy density li metal dual-ion battery with a lithium nitrate-modified carbonate-based electrolyte, ACS Appl. Mater. Interfaces 11 (2019) 18504-18510.

(51) T.F. Yi, Y. Xie, Y.R. Zhu, R.S. Zhu, M.F. Ye, High rate micron-sized niobium-doped $LiMn_{1.5}Ni_{0.5}O_4$ as ultra high power positive-electrode material for lithium-ion batteries. J. Power Sources 211 (2012) 59-65.

(52) Y.F. Deng, S.X. Zhao, Y.H. Xu, K. Gao, C.W. Nan, Impact of P-doped in spinel $LiNi_{0.5}Mn_{1.5}O_4$ on Degree of Disorder, grain morphology, and electrochemical performance, Chem. Mater. 27 (2015) 7734-7742.

(53) J.H. Kim, S.T. Myung, C.S. Yoon, I.H. Oh, Y.K. Sun, Effect of Ti substitution for mn on the structure of $LiNi_{0.5}Mn_{1.5-x}Ti_xO_4$ and their electrochemical properties as lithium insertion material, J. Electrochem. Soc. 151 (2004) A1911-1918.

(54) G.B. Zhong, Y.Y. Wang, Z.C. Zhang, C.H. Chen, Effects of Al substitution for Ni and Mn on the electrochemical properties of $LiNi_{0.5}Mn_{1.5}O_4$, Electrochim. Acta 56 (2011) 6554-6561.

(55) S. Nageswaran, M. Keppeler, S.J. Kim, M. Srinivasan, Morphology controlled Si-modified $LiNi_{0.5}Mn_{1.5}O_4$ microspheres as high performance high voltage cathode materials in lithium ion batteries, J. Power Sources 346 (2017) 89-96.

(56) S.H. Oh, K.Y. Chung, S.H. Jeon, C.S. Kim, W.I. Cho, B.W. Cho, Structural and electrochemical investigations on the $LiNi_{0.5-x}Mn_{1.5-y}M_{x+y}O_4$ (M=Cr, Al, Zr) compound for 5 V cathode material, J. Alloys Compd. 469 (2009) 244-250.

(57) P.J. Kumar, K. Nishimura, M. Senna, A. Düvel, P. Heitjans, T. Kawaguchi, N. Sakamoto, N. Wakiya, H. Suzuki, A novel low-temperature solid-state route for nanostructured cubic garnet $Li_7La_3Zr_2O_{12}$ and its application to li-ion battery, RSC Adv. 6 (2016) 62656-62667.

(58) A. Castillo, T. Charpentier, O. Rapaud, N. Pradeilles, S. Yagoubi, E. Foy, M. Moskura, H. Khodja, Bulk Li mobility enhancement in spark plasma sintered $Li_{(7-3x)}Al_xLa_3Zr_2O_{12}$ garnet, Ceram. Inter. 44 (2018) 18844-18850.

(59) X. Liu, J. Tan, J. Fu, R. Yuan, H. Wen, C. Zhang, Facile synthesis of nanosized lithium-ion-conducting solid electrolyte $Li_{1.4}Al_{0.4}Ti_{1.6}(PO_4)_3$ and Its Mechanical Nanocomposites with $LiMn_2O_4$ for enhanced cyclic performance in lithium ion batteries, ACS Appl. Mater. Interfaces 9 (2017) 11696-11703.

(60) H.V. Ngoc, C.I. Jong, U. Sanjith, B.I. Won, Synergic coating and doping effects of Ti-Modified Integrated Layered–Spinel $Li_{1.2}Mn_{0.75}Ni_{0.25}O_{2+\delta}$ as a high capacity and long lifetime cathode material for li-ion batteries, J. Mater. Chem. A 6 (2018) 2200-2211.

(61) R.P. Qing, J.L. Shi, D.D. Xiao, X.D. Zhang, Y.X. Yin, Y.B. Zhai, L. Gu, Y.G. Guo, Enhancing the kinetics of Li-rich cathode materials through the pinning effects of gradient surface Na^+ doping. Adv. Energy Mater. 6 (2016) 1501914-1501920.

(62) W. Liu, Q. Shi, Q. Qu, T. Gao, G. Zhu, J. Shao, H. Zheng, Improved Li-ion diffusion and stability of a $LiNi_{0.5}Mn_{1.5}O_4$ cathode through in situ Co-doping with dual-metal cations and incorporation of a superionic conductor, J. Mater. Chem. A *5* (2017) 145-154.

(63) R. Zhao, L. Li, T.H. Xu, D. Wang, D. Pan, G.J. He, H.L. Zhao, Y. Bai, One-step integrated surface modification to build a stable interface on high-voltage cathode for lithium-ion batteries, ACS Appl. Mater. Interfaces 11 (2019) 16233-16242.

(64) X. Zheng, W. Liu, Q. Qu, H. Zheng, Y. Huang, Bi-functions of titanium and lanthanum co-doping to enhance the electrochemical performance of spinel $LiNi_{0.5}Mn_{1.5}O_4$ cathode, Journal Materics. 5 (2019) 156-163.

(65) H. Yang, H.H. Wu, M. Ge, L. Li, Y. Yuan, Q. Yao, J. Chen, L. Xia, J. Zheng, Z.

Chen, J. Duan, K. Kisslinger, X.C. Zeng, W.K. Lee, Q. Zhang, J. Lu, Simultaneously dual modification of Ni-Rich layered oxide cathode for high‐energy lithium‐ion batteries, Adv. Funct. Mater. 29 (2019) 1808825-1808838.

(66)J.H. Kim, S.T. Myung, C.S. Yoon, S.G. Kang, Y.K. Sun, Comparative study of $LiNi_{0.5}Mn_{1.5}O_{4-\delta}$ and $LiNi_{0.5}Mn_{1.5}O_4$ cathodes having two crystallographic structures: Fd3m and $P4_332$. Chem. Mater. 16 (2004) 906-914.

(67) L.N. Wan, Y.F. Deng, C.X. Yang, H. Xu, X.S. Qin, G.H. Chen, Ni/Mn ratio and morphology-dependent crystallographic facet structure and electrochemical properties of the high-voltage spinel $LiNi_{0.5}Mn_{1.5}O_4$ cathode material, RSC Adv. 5 (2015) 25988-25997.

(68)N. Amdouni, K. Zaghib, F. Gendron, A. Mauger, C.M. Julien, Structure and insertion properties of disordered and ordered $LiNi_{0.5}Mn_{1.5}O_4$ spinels prepared by wet chemistry. Ionics 12 (2006) 117-126.

(69) J.M. Zheng, J. Xiao, X.Q. Yu, L. Kovarik, M. Gu, F. Omenya, X.L. Chen, X.Q. Yang, J. Liu, G.L. Graff, M.S. Whittingham, J.G. Zhang, Enhanced Li+ ion transport in LiNi0.5Mn1.5O4 through control of site disorder, Phys. Chem. Chem. Phys. 14 (2012) 13515-13521.

(70)D.D. Wang, T. Xu, Y. Li, D. Pan, X. Lu, Y.S. Hu, S. Dai, Y. Bai, Integrated surface functionalization of Li-rich cathode materials for Li-ion batteries, ACS Appl Mater Interfaces 10 (2018) 41802-41813.

Table 1 EIS Fitting data of the pristine and LLAZO-1 samples.

	Resistance	1st	10th	20th	30th
Pristine	Rsf	84	122	167	226
	Rct	352	432	595	648
LLAZO-1	Rsf	113	179	202	233
	Rct	171	208	218	254

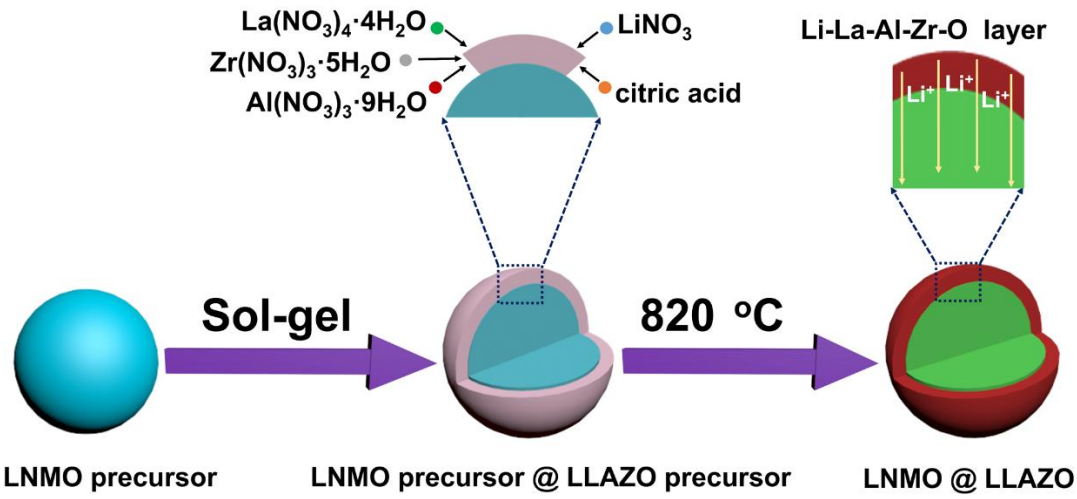

Figure 1. Schematic illustration of the synthesis process for LLAZO-modified LNMO.

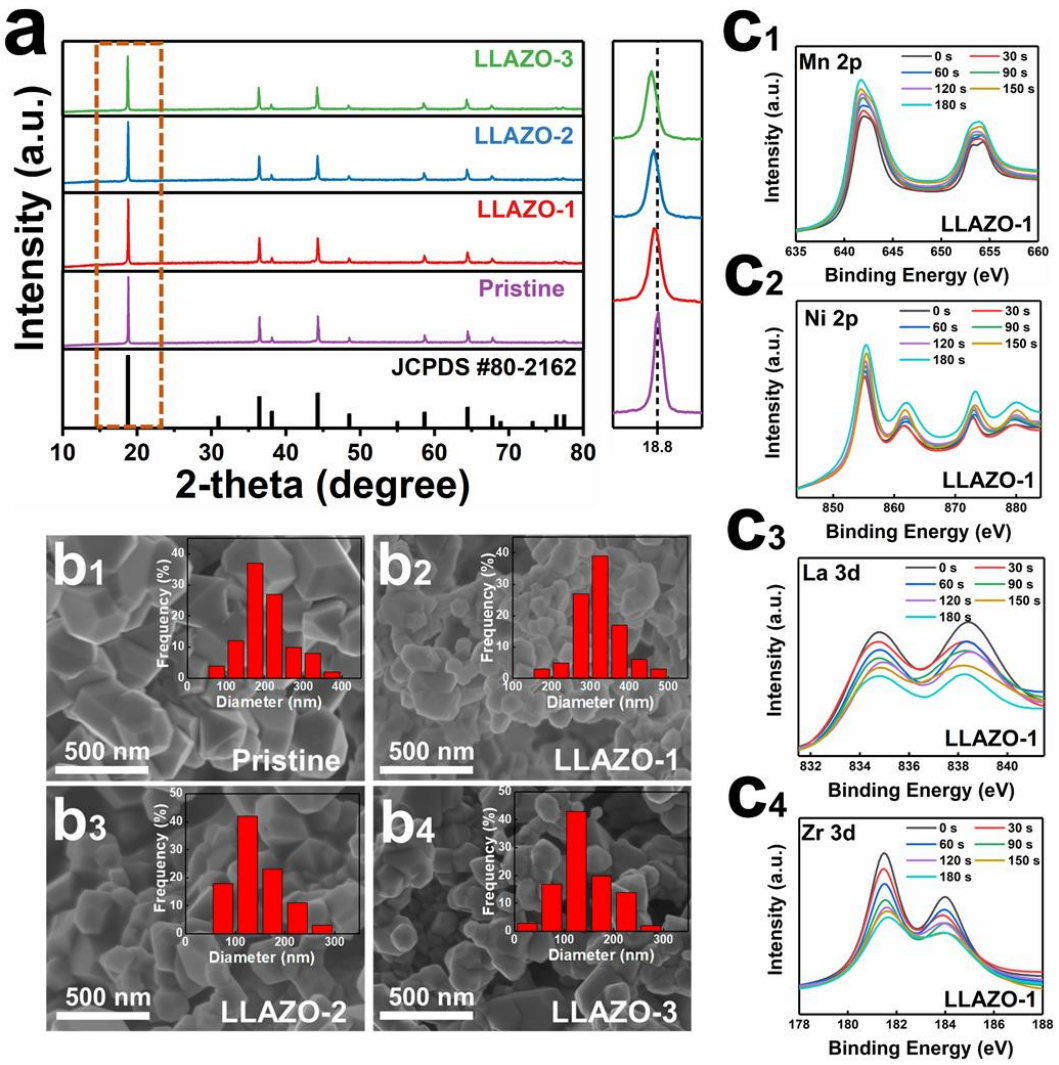

Figure 2. (a) XRD patterns of the pristine and LLAZO-modified LNMO samples, SEM of (b_1) pristine, (b_2) LLAZO-1, (b_3) LLAZO-2, (b_4) LLAZO-3, and the XPS sputtered depth profiles of (c_1) Mn 2p (c_2) Ni 2p (c_3) La 3d and (c_4) Zr 3d in the LLAZO-1 along with etching times.

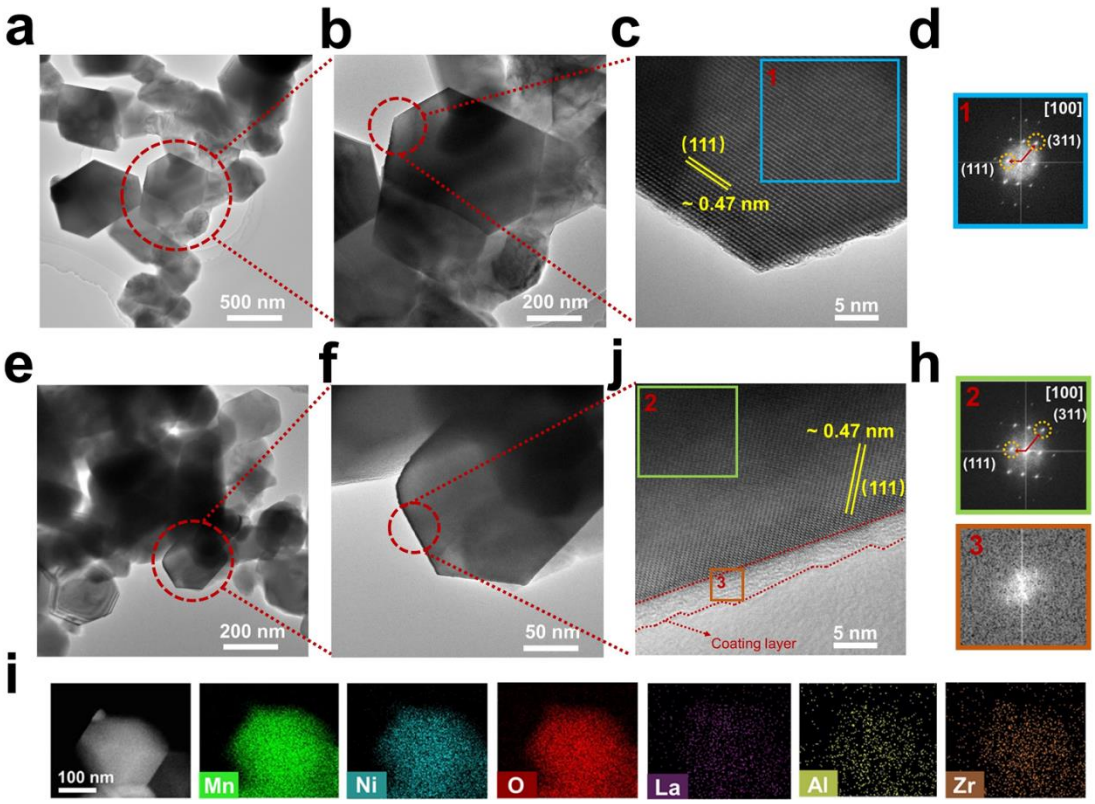

Figure 3. TEM and HRTEM images of (a, b and c) pristine LNMO and (e, f and j) LLAZO-1, respectively. (d, h) FFT patterns of marked region 1 in (c), and 2 and 3 in (j), respectively. (i) EDS elemental maps of LNMO-1LLAZO.

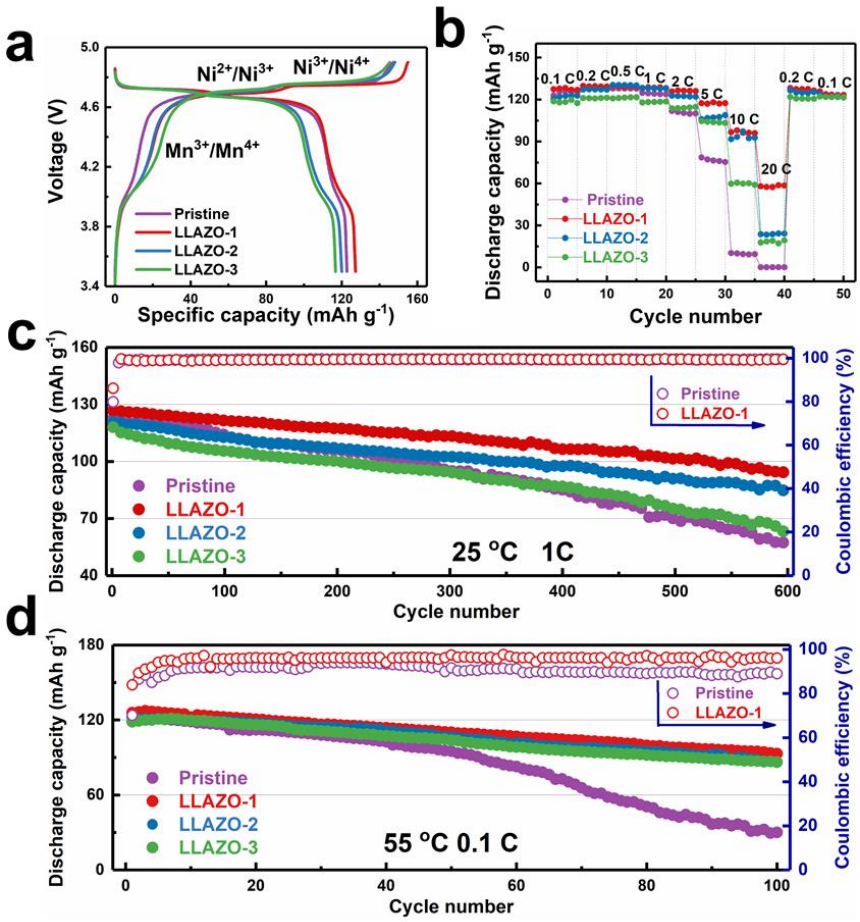

Figure 4. (a) Initial charge-discharge profiles of all samples, (b) rate capabilities of all electrodes at various discharge rates, (c) cycling performances of samples at 25 ºC, (d) cycling performances of samples at a high temperature of 55 ºC.

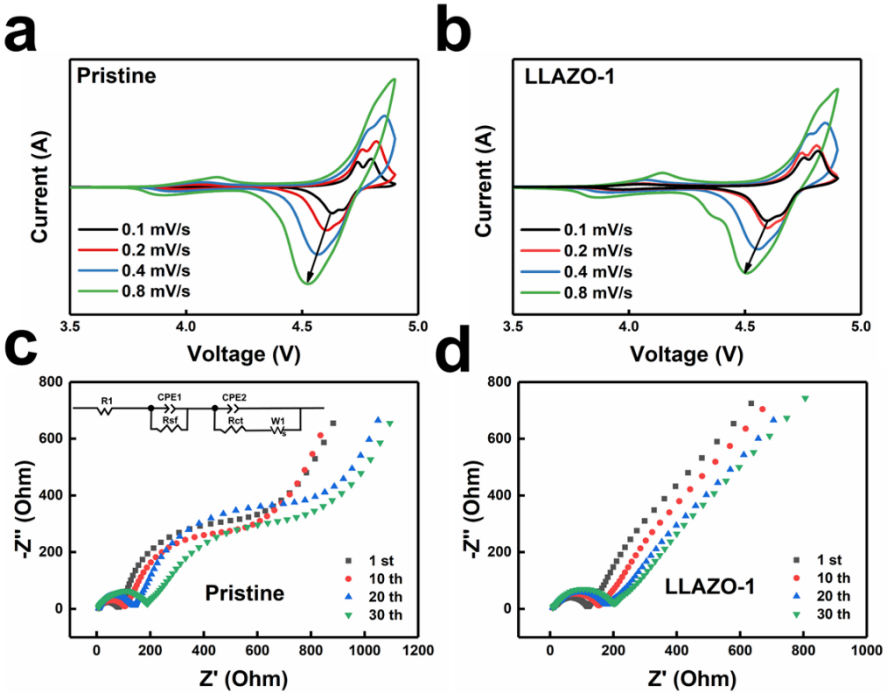

Figure 5. CV curves of (a) pristine and (b) LLAZO-1 under different scan rates; and the Nyquist plots of (c) pristine and (d) LLAZO-1 at different cycles.

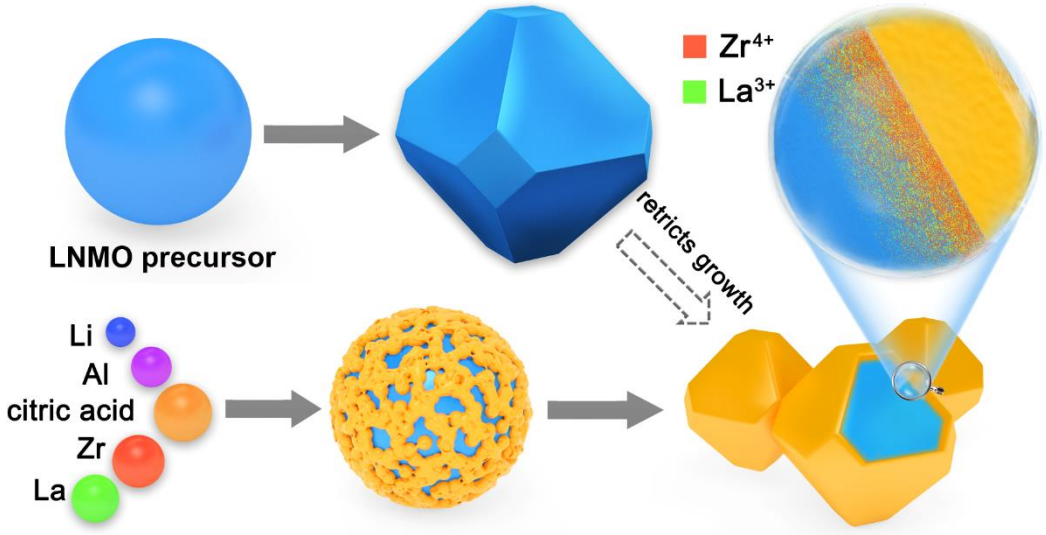

Figure 6. Schematic illustration of the tri-functional effects of LLAZO modified LNMO cathode material.